EES Catalysis

PAPER

View Article Online
View Journal | View Issue

Cite this: *EES Catal.*, 2023, 1, 263

Local hydrophobicity allows high-performance electrochemical carbon monoxide reduction to C_{2+} products†

Attila Kormányos,[a] Balázs Endrődi,*[a] Zheng Zhang,[a] Angelika Samu,[a] László Mérai,[a] Gergely F. Samu,[ab] László Janovák[a] and Csaba Janáky*[ab]

Received 13th January 2023,
Accepted 4th March 2023

DOI: 10.1039/d3ey00006k

rsc.li/eescatalysis

While CO can already be produced at industrially relevant current densities *via* CO_2 electrolysis, the selective formation of C_{2+} products seems challenging. CO electrolysis, in principle, can overcome this barrier, hence forming valuable chemicals from CO_2 in two steps. Here we demonstrate that a mass-produced, commercially available polymeric pore sealer can be used as a catalyst binder, ensuring high rate and selective CO reduction. We achieved above 70% faradaic efficiency for C_{2+} products formation at j = 500 mA cm^{-2} current density. As no specific interaction between the polymer and the CO reactant was found, we attribute the stable and selective operation of the electrolyzer cell to the controlled wetting of the catalyst layer due to the homogeneous polymer coating on the catalyst particles' surface. These results indicate that sophistically designed surface modifiers are not necessarily required for CO electrolysis, but a simpler alternative can in some cases lead to the same reaction rate, selectivity and energy efficiency; hence the capital costs can be significantly decreased.

Broader context

Electrochemical power-to-gas and power-to-liquid technologies are promising chemical energy conversion approaches to be coupled with intermittent renewable energy sources. As the flagship, the electrochemical production of hydrogen from water electrolysis *via* PEM electrolyzers has already reached the market. The electrochemical reduction of CO_2 builds on this knowledge, and therefore a rapid development of cell structures and cell constituents was witnessed in recent years. Production of CO through CO_2 reduction seems to be feasible even at a pilot scale, but the selective production of high-value multi-carbon products is challenging. CO reduction is a possible second step in the cascade electrochemical valorization of CO_2, offering a possibility to produce further reduced, higher value products, such as different alcohols, methane, or ethylene. Gas-phase electrolyzers offer a suitable platform for this process, but the low solubility of CO poses notable challenges. This can be tackled by tailoring the microenvironment of the catalyst particles, and thereby high conversion rates and product selectivity could be achieved.

Introduction

Electrochemical transformation of carbon dioxide (CO_2RR) and carbon monoxide (CORR) is an attractive alternative to the Fischer–Tropsch method to form valuable chemicals, such as ethylene, ethanol, or acetic acid.[1,2] CORR can be performed at low temperature and pressure, and it is expected to be just as scalable as other electrolysis technologies, therefore allowing the de-centralized operation of smaller CO processing plants. A further benefit of electrochemical technologies is that intermittently available renewable electricity can be directly utilized to produce valuable products.[3–5]

Two electron products, namely formic acid (formate) and CO can be produced *via* CO_2RR with high selectivity and at a high rate.[6–8] Such devices are currently entering the pilot scale and are expected to be industrialized within a decade. The direct production of C_{2+} products from CO_2 is, however, hampered by the low process selectivity. CO is generally accepted to be an intermediate during CO_2RR to further reduced products.[9] We envision that a two-step electrolysis process (*i.e.*, CO_2 → CO → C_2 products) can result in higher selectivity and reaction rates, as optimized electrocatalysts and reaction environments can be applied for the two consecutive reaction steps.[1] Also, during CO_2RR, a large amount of the reactant CO_2 is lost due to carbonate formation (with the loss scaling with the e$^-$ number

[a] *Department of Physical Chemistry and Materials Science, University of Szeged, Aradi sq. 1, Szeged, 6720, Hungary. E-mail: endrodib@chem.u-szeged.hu, janaky@chem.u-szeged.hu*

[b] *ELI-ALPS, ELI-HU Non-Profit Ltd., Wolfgang Sandner 3, Szeged H-6728, Hungary*

† Electronic supplementary information (ESI) available. Experimental procedures and results, Fig. S1–S17 and Tables S1, S2. See DOI: https://doi.org/10.1039/d3ey00006k

used to form a specific product).[10] This loss can be only avoided by applying special separators (*i.e.*, bipolar membranes) or electrolyzer cells of special design (*e.g.*, having a liquid layer between two membranes)[11] that typically come at a high price in terms of low energy efficiency.[12] CO_2 loss to the electrolyte solution(s) increases the operating costs of the process, as this has to be recovered from a gas mixture (typically CO_2/O_2) if high conversions are the focus of the technology. Such an issue is not relevant during CORR, and therefore the reactant loss is minimal in this case.

Since the initial studies on different metal electrodes,[13,14] several catalysts were investigated in CORR. Similarly to CO_2RR, copper is the only catalyst for C_{2+} product formation in CORR that shows reasonable performance.[2,15–17] This is rooted in the optimal binding energies of the reaction intermediates on copper. The reaction rate and selectivity are also highly dependent on the catalyst morphology and the dominantly available crystal facets, attracting notable attention to catalyst design, such as synthesizing Cu nanocubes, which achieve very high ethylene selectivity in CO_2RR.[18–20] The mechanism of CORR has been studied *via* experimental and theoretical means in multiple accounts,[21–23] but some uncertainties remain. It is, however, clear from these works that CO adsorption, hydrogenation, and C–C coupling reactions occur at the catalyst surface. Theoretical studies on CO_2RR suggest that tri- and tetraalkylammonium groups can promote the reaction by binding certain intermediates.[24,25] As CO is a generally considered key intermediate in CO_2RR, these studies are relevant for CORR as well. As for CORR, small molecule tetraalkylammonium ions were proved to affect the reaction. Hence, a similar effect of ammonium groups can be envisioned as for CO_2RR.[26] Furthermore, the promoting effect of alkali cations at the catalyst surface was proved, similarly to the case of CO_2RR,[27–29] and thus, the presence of these is also necessary for efficient CORR.[30] Therefore, beyond the composition and morphology of the catalyst material (with appropriate active site spacing[31]), its local chemical environment also strongly affects the reaction rate and selectivity. Clearly, CO and a proton source (*i.e.*, H_2O) must be simultaneously present at the electrode surface. Notably, the solubility of CO is *ca.* 30 times lower as compared to that of CO_2. Ensuring a short diffusion length (*i.e.*, very thin water layer at the catalyst surface) during CO_2RR was shown to be critical for achieving high reaction rates, and that is even more emphasized in the case of CORR.[32] In short, a situation as close to the often-mentioned triple-phase boundary conditions as possible should be achieved.

To allow the proper transport of the CO reactant, gas-fed electrolyzer cells must be used, applying gas diffusion electrodes (GDEs).[33] In these architectures, the catalyst layer (CL) is immobilized on a hydrophobic porous substrate (gas diffusion layer, GDL) that allows the gas to reach the catalyst surface and ensures the separation of the gas and liquid phases. The CL is in direct contact with a solid (in zero-gap cells) or a liquid electrolyte (in microfluidic electrolyzer cells) from the other side. The composition of the CL influences the reaction zone between the reactant gas (CO in this case), water, and the catalyst nanoparticles, directly affecting the rate and selectivity of the process.[34] CLs formed of metal nanoparticles without any additive can be hydrophobic,[35] and therefore, CORR can be initially pursued. Under relevant reaction conditions, however, this might change (*i.e.*, because of electrowetting or wetting by the formed products).[36] When water enters the CL in large amounts (forming a thick hydration shell around the catalyst particles), it blocks the reactant gas from the catalyst particles, leading to a suddenly increasing HER selectivity.[37] Such flooding of the GDE is typically irreversible and is associated with the loss of hydrophobicity of the GDE. As it was demonstrated already for CO_2RR, the reaction selectivity gradually decreases, and the parasitic hydrogen evolution reaction (HER) becomes dominant when flooding occurs.[38]

The surface modification of the catalyst particles with polymeric materials or (large) molecules is an increasingly applied strategy in CO_2RR studies, allowing to tune the hydrophobicity of the catalytic surface.[39–43] Such polymer materials are most often employed as catalyst binders, immobilized together with the catalyst particles during GDE formation. These include Nafion, other fluorinated polymers, or electrically conducting polymers.[44–47] The requirements for a possible binder material are to increase the hydrophobicity of the CL, remain stable under electrolysis conditions, mechanically separate (stabilize) the catalyst nanoparticles, and bind them strongly to the electrode support without blocking the gas transport to the catalyst particles. As a further possible benefit, the binder can also act as a co-catalyst (or reaction promoter) in the reaction by regulating the surface pH,[48] changing the surface electronic properties of the catalyst,[43] and/or adsorbing/activating the reactant.[49] This latter is typically achieved *via* tailored functional groups (*e.g.*, N-moieties), aiding the adsorption of the reactants and/or intermediates. Interestingly, despite the favorable properties of such additives, their use is much less explored and understood in CORR, compared to CO_2RR.

In this contribution, we present that a mass-produced, commercially available pore-sealer fluoropolymer (Capstone ST-110 latex) can act as a catalyst binder, ensuring high rate CORR to C_{2+} products. We demonstrate that this polymer binder has excellent film-forming ability and, at optimal loadings, covers the surface of the catalyst particles. This ensures that no thick water films form around the catalyst nanoparticles, which would block the path of CO gas. Consequently, hydrogen evolution can be suppressed while acetate, ethanol, ethylene (C_2 products), and even propanol form at a high rate.

Experimental

Materials

All chemicals used in this study were purchased from Merck or VWR International. Chemicals of high purity (at least ACS reagent grade) were purchased and used without further purification. An aqueous dispersion of Capstone ST-110, was purchased from Chemours. Aqueous PTFE dispersion was from Merck, while 10 wt% aqueous Nafion dispersion was purchased

from Fuel Cell Store. Ultrapure water (18.2 MΩ cm) was used for the experiments, freshly produced using a Millipore Direct Q3 UV instrument. A 4.7 purity CO (from Messer) cylinder was used for the CORR studies.

Methods

All electrodes were formed by spray-coating the catalyst dispersion on Freudenberg H23C6 GDLs, preheated on a hot-plate at T = 100 °C. Copper nanoparticles (d_{avg} = 25 nm, Sigma-Aldrich) were dispersed in a 1 : 1 isopropanol/water mixture at a concentration of 25 mg cm^{-3}. Capstone ST-110 binder was added to the Cu nanoparticle dispersion in different amounts (expressed in wt%, related to the total mass of the catalyst and the binder). Nafion-, and PTFE-containing dispersions and GDEs were prepared identically to the CST-containing ones. As for the anode catalyst, IrO_x nanoparticles (Fuel-Cell Store) were dispersed in a 1 : 1 isopropanol/water mixture with 15 wt% Nafion ionomer content at a concentration of 20 mg cm^{-3}. The IrO_x dispersion was homogenized in a regular ultrasonic bath for 20 min (keeping the bath temperature below 35 °C), while a high-power immersion sonotrode was used to disperse the Cu nanoparticles.

Continuous-flow electrolysis experiments were performed in a two-electrode setup in a microfluidic cell, designed based on the work of the Kenis research group.[50,51] This consisted of stainless steel (1.4571, 316-Ti) electrodes and a poly(methyl methacrylate) (PMMA) separator (d = 2 mm thickness). 3 mm deep, 2 cm × 0.5 cm large cavities were formed on the metal electrodes to serve as gas flow channels. Threaded M5 inlet and outlet connection ports were formed on the cathode for CO transport, while a similar single outlet port was constructed on the anode to allow the evolving O_2 to leave the cell. A 2 cm × 0.5 cm large opening was created in the middle of the PMMA separator, defining A = 1 cm^2 electrolysis geometric area. ∅ = 1 mm holes were drilled in two opposite sides of this plastic element, going through the middle of the opening, for the transport of the electrolyte solution. The connection of the liquid pump was established by mounting 1 mm needles in the holes. The cathode GDE and the PTFE gasket (d = 100 μm thickness) around it were placed between the cathode electrode and the PMMA separator. The anode was mounted in the cell similarly. CO gas was fed to the cathode in a flow-by mode at a rate of u = 26.5 sccm through a ∅ = 6 mm polyurethane tube (Festo), while an electrolyte solution was directed between the two electrodes through a ∅ = 4 mm polyurethane tube (Festo) and the needles mounted in the flow channel at a flow rate of 0.5 cm^3 min^{-1}. A Bronkhorst EL-FLOW Select F-201CV mass flow controller and a KF Technology NE-300 syringe pump was used for regulating the gas and the liquid flow rates, respectively.

The electrochemical measurements were controlled using a Biologic VMP300 type instrument. The CORR products were monitored during the electrolysis using a Shimadzu Nexis GC-2030 gas-chromatograph (operated with 6.0 He carrier gas), equipped with a barrier discharge ionization (BID) detector, and an automated 6-way valve injection system. Faradaic efficiency of the CO electrolysis was calculated from the GC results and the measured gas flow rate (Agilent ADM flow meter). Importantly, the pressure increase in the gas line – that could lead to electrode flooding – was avoided by applying a small vacuum pump to fill the sample loop of the injector, sampling the main gas stream.

An atmospheric mass spectrometer (SRS UGA200) was also used to monitor the reaction products and to readily confirm the flooding of the cathode, indicated by the rapid increase in the hydrogen evolution rate. The liquid phase CORR products were quantified using a Bruker AV-III-500-HD NMR instrument after performing a calibration for the studied compounds (with the same background electrolyte concentration as in the real samples). DMSO and phenol were used as internal standards.[52]

A Thermo Scientific Apreo 2 scanning electron microscope (SEM) was used to collect information on the morphology of the formed electrodes. Top-down and cross-section scanning electron microscopy (SEM) images were recorded with a Thermo Scientific Scios 2 SEM-FIB instrument. A FEI Tecnai G2 20 X-Twin type instrument, operating at an acceleration voltage of 200 kV, was used for recording transmission electron microscopy (TEM) images. An EasyDrop (Krüss) type instrument was used to measure the wetting properties of the different Capstone ST-110 containing GDEs, formed on Freudenberg H23C6 GDLs. A V = 10 μl drop of 1 M KOH solution was formed on the GDE using a syringe with a PTFE lined syringe. Using the CCD camera of the goniometer, the drop contour of the captured photographs was analyzed based on the Young–Laplace equation using the DSA100 software. The contact angles (Θ) were determined as the slope of the contour line at the three-phase contact point. Dynamic contact angle measurements were performed using the same device, first forming a continuously growing droplet (advancing contact angle) and then gradually pulling the liquid back into the syringe (receding contact angle). The gas adsorption properties of Capstone ST-110 films were monitored in quartz crystal microbalance (QCM) experiments using an SRS QCM200 instrument and gold-coated quartz crystal (f_0 = 5 MHz). The mass change was calculated from the Sauerbrey equation ($\Delta f = -C \times \Delta m$), using a constant value of C = 56.6 Hz μg^{-1} cm^2 as provided in the manual of the instrument.

Results and discussions

Morphological and physical characterization of the formed GDEs

Commercially available copper nanoparticles (Cu NPs, d < 25 nm) were applied as cathode catalyst and immobilized by spray-coating on a carbon paper support to form GDEs. Capstone ST-110 (referred to as CST in what follows) was employed as a catalyst binder and surface modifier in the catalyst layers. CST was added to a catalyst dispersion in varying amounts (expressed as wt%, related to the total mass of the catalyst + binder) and was immobilized on the carbon paper together with the Cu NPs *via* spray-coating.

The morphology of the prepared GDEs was studied by cross-section SEM. To avoid the distortion of the GDE structure

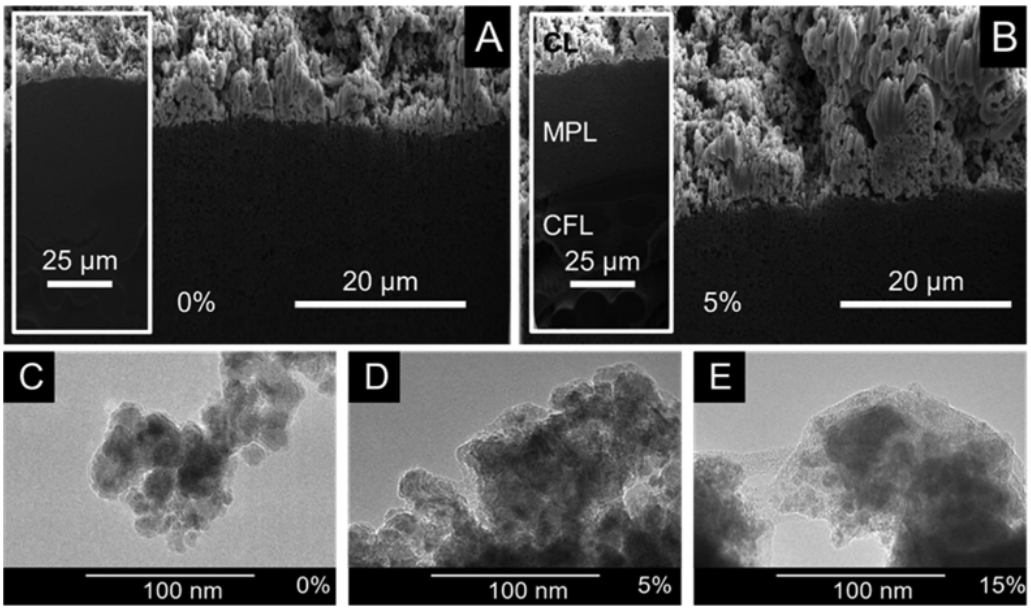

Fig. 1 FIB-SEM images of (A) Cu NPs and (B) Cu NPs + CST (5 wt%) containing GDEs on a Freudenberg H23C6 carbon paper. The Cu loading was fixed at 1 mg cm^{-2} in the case of both samples. The inset images were taken at a lower magnification to capture the whole structure of the GDE. CFL – carbon fiber layer, MPL – microporous layer, CL – catalyst layer. TEM images captured for pristine Cu NPs (C) and Cu NPs + CST (5 wt% (D) and 15 wt% (E)).

(that inevitably happens when a blade is used), a ditch was formed in the GDE by focused ion beam (FIB) technique applying Ga ions. Fig. 1A shows the cross-section SEM image captured from the GDE containing no binder. The thickness of the CL shows notable irregularities in the range of 5–20 μm. This might be due to the absence of the ionomer that might help keeping the nanoparticles in the dispersion and preventing their rapid aggregation. Even if this is the case, it is not reflected in the cross-section image taken from the GDE containing 5 wt% CST (Fig. 1B). The CL appears to be slightly thicker however, the presence of the polymer binder cannot be unequivocally identified (the ion beam used for the cleaning of the freshly etched surface might ''burned'' the CST at the surface). To better visualize the presence of CST in the CL, top-down SEM images were captured from each Cu/CST GDE with varying CST content (Fig. S1, ESI†). The apparent diameter of the Cu NPs gradually increased with the amount of CST in the CL (5–15 wt%), indicating a polymer shell formation on the nanoparticles. When the CST loading reached 20 wt%, the binder started to form a coherent film on top of the catalyst layer sticking together the Cu NPs. At 30 wt% CST content, almost only the CST film is visible beside a few protruding catalyst nanoparticles.

TEM images (Fig. 1C–E) confirmed the same notion: aggregated Cu NPs ($d_{average} \approx 12$ nm based on TEM images presented in Fig. S2, ESI†) were seen in the absence of the binder, while a thickening polymer layer (a light-grey shell) around the particles was found with the increasing CST concentration. The excess amount of the polymer might penetrate into the pores and/or form a surface film on top of the catalyst layer. We mention here that CST is a commercial pore-sealer material, and therefore this effect is not unexpected. In fact, this motivated our choice of material when we aimed to modify the hydrophilic/hydrophobic nature of our GDE.

CST is a terpolymer of fluorinated alkyl-methacrylates, dialkylammoniumalkyl methacrylate acetate salts, and aliphatic acids, but its exact composition is a trade secret and is therefore not shared with the end-user. An interesting feature, however, is the trialkylammonium group (Fig. S3, ESI,† when protonated), a motif that resembles what is typically present in anion exchange polymers (employed as membranes and ionomers) as well.[53,54] Such functional groups were shown to bind CO_2, aiding CO_2RR, and therefore its participation in the electrolysis process was suggested.[55] To reveal any similar interaction between the CST polymer and the CO reactant, quartz crystal microbalance (QCM) experiments were performed (Fig. S4, ESI†). No mass change was detected when Ar or CO gas was purged in the gas chamber over the CST-coated QCM crystal. This shows that the most important role of the CST polymer is not to bind the reactant. Interestingly, a notable mass increase was witnessed when repeating the QCM experiments in CO_2 atmosphere. Based on these experiments, no specific contribution of the binder in CORR is expected, while it might assist high-rate CO_2RR by binding CO_2, thereby increasing its concentration in the immediate vicinity of the catalyst particles.

The hydrophobic/hydrophilic character of freshly prepared GDEs formed of Cu NPs and different amounts of CST were evaluated by contact angle measurements, applying a 1 M KOH solution (Fig. 2A). Here, the binder-free sample was wetted well by the solution ($\Theta = \sim 65^\circ$), but a much higher contact angle was measured for all the CST containing GDEs ($140 \pm 5^\circ$), proving the increased hydrophobic character of these layers. We mention that when using pure water as the wetting solution

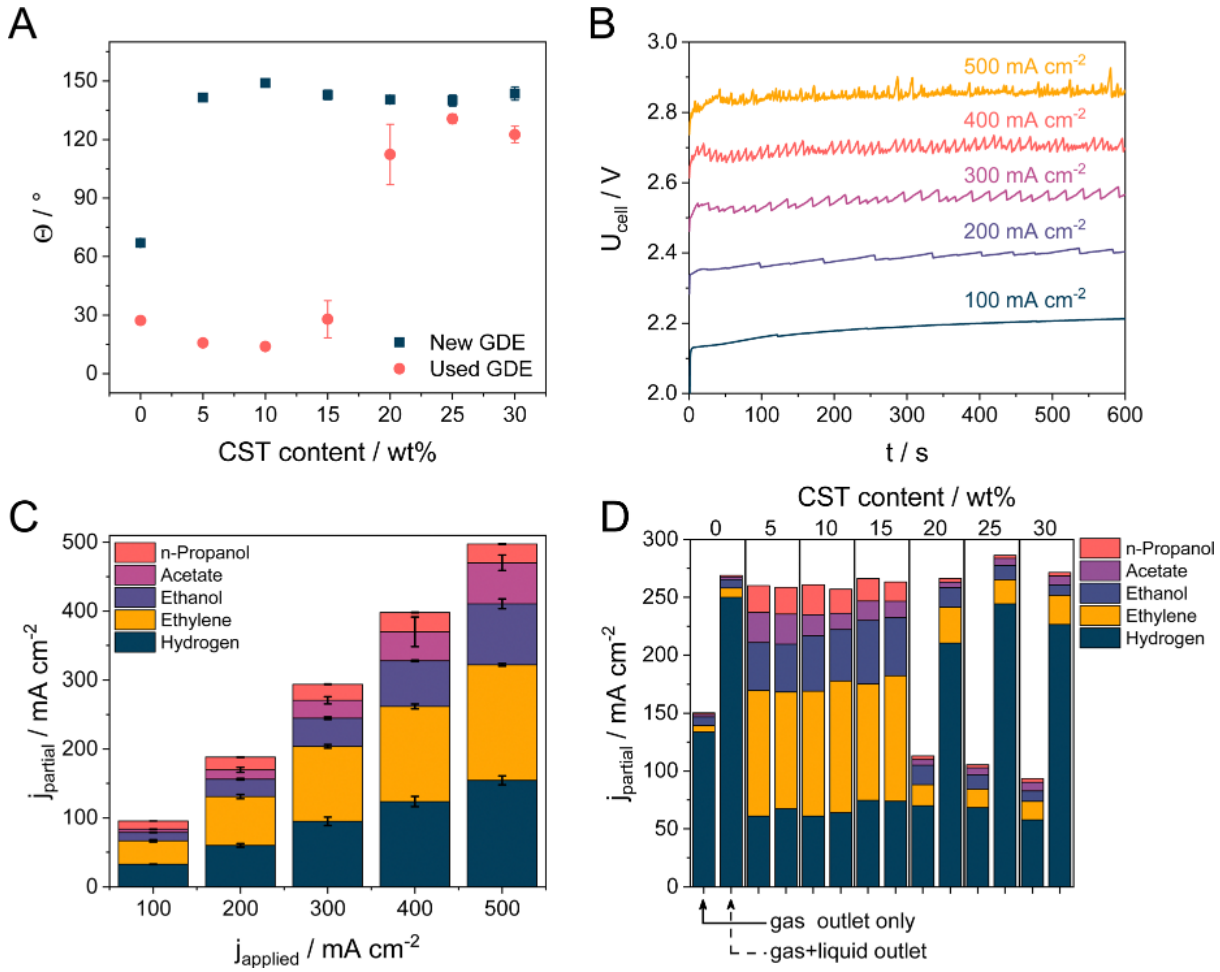

Fig. 2 (A) Contact angles of 1 M KOH droplets at Cu NPs-GDE with varying Capstone content (5–30 wt%). (B) Cell voltage recorded for Cu NPs + 5 wt% CST sample during electrolysis performed at 100–500 mA cm^{-2} current densities in 1 M KOH electrolyte solution at room temperature. The electrolyte flow rate was 0.5 cm^3 min^{-1}, while the CO flow rate was 26.5 sccm. All chronovoltammetric measurements were performed on the same electrode. (C) Product distribution at different current densities with 5 wt% CST containing GDEs. Error bars were calculated from at least two individual measurements. (D) Product distribution was obtained at 300 mA cm^{-2} current density using Cu NPs-coated GDE with varying CST content. The amount of the formed products were either determined only from the gas outlet stream (left column in each case) or by connecting the gas and liquid outlet stream after a water separator (right column in each case). For further information, see Fig. S10 (ESI†).

(that is the practice in most studies), no differences were found among the different GDEs, even the CST-free sample was superhydrophobic (with a contact angle above 160°). We note here that surface wetting depends the most on the nature of the solvent, but it can also be affected by the solution pH and the ionic strength (see Fig. S5 for a set of experiments demonstrating this effect, ESI†).

Electrocatalytic reduction of carbon monoxide

The electrocatalytic activity of the Cu NP GDEs, containing different amounts of CST, was studied in a microfluidic electrolyzer cell (Fig. S6, ESI†). Chronovoltammetry experiments were performed at five current densities between j = 100–500 mA cm^{-2}, consecutively measured on the same electrode (as opposed to numerous studies in the field). In the case of the 5 wt% CST containing electrode, the cell voltage is almost linearly scaled with the current density between U_{cell} = 2.2 – 2.85 V (Fig. 2B). Higher cell voltages were recorded with GDEs containing a higher amount of CST (*ca.* 3.25 V at j = 500 mA cm^{-2} with the highest studied polymer amount, see Fig. S7, ESI†). This cell voltage increase is rooted in the increasing electrical resistance of the layers, caused by the increase in the incorporated amount of a non-conducting polymer. Additionally, the chronovoltammetry curves became noisier due to the increasing bubble formation at higher current densities. Fig. 2C shows the product distribution during the CORR for the cathode GDE containing 5 wt% CST. Product distribution as the function of the CST content is presented in Fig. S8 (ESI†). Faradaic efficiencies (FE) for all product distribution data presented in this manuscript are collected in the ESI† in Table S2. We identified four CO reduction products, namely ethylene, ethanol, acetate, and *n*-propanol, and confirmed the formation of H_2 as a by-product. A small amount of methane was also detected, but only in the case of the pristine sample and only at 400 and 500 mA cm^{-2} current density. We assume that this is related to

the changing catalyst morphology during electrolysis,[56] but the detailed investigation of this is beyond the scope of our current study. H_2 was the main product in the case of using CST-free GDEs. A low amount of ethylene formed in this case at lower current densities, but no ethylene formed at higher current densities.

Importantly, even the smallest amount (5 wt%) of CST in the catalyst layer has a huge effect on the selectivity; the amount of H_2 decreased while the faradaic efficiency (FE) for ethylene formation increased to 32–37%, along with a notable increase in the amount of the formed liquid C_{2+} products. The FE for ethanol formation reached 18% at 500 mA cm^{-2} current density (around 90 mA cm^{-2} partial current density), while this value was 12% for acetate and around 5.5% for *n*-propanol, respectively. The measured product distribution is in the range of the best-published examples in the literature using Cu NPs (either commercially available or custom-synthesized) as the cathode catalyst.[1,17,57] Interestingly, the product distribution seems to be almost independent of the applied current density, although, based on the approximately 700 mV shift in the cell voltage, it should alter the ratio of the formed CORR products. To scrutinize this behavior further, a small reference electrode was introduced in the electrolyte compartment of the cell (Fig. S9A, ESI†) in the close vicinity of the cathode (~1 mm distance), and the cathode potential was monitored in parallel with the cell voltage (Fig. S9B, ESI†). Although the uncompensated cathode potential (and hence the cell voltage) changes gradually with the applied current density, the IR-corrected (series resistance values for each applied current density are presented in Table S1, ESI†) cathode potential remains almost constant, the change is less than 50 mV. This very narrow potential regime explains why the product distribution seems identical at the different current densities. We mention that despite this slight difference between the measured cathode potentials, the product distribution slightly depends on the applied current density, for further information, please refer to Table S2 (ESI†).

Selectivity towards C_{2+} product formation remains similar for the GDEs containing 10 wt% CST and only slightly decreases when the CST content is further increased to 15 wt%. In terms of the total FE (Fig. S10, ESI†), we can account for approximately 85–95% of the passed charge. We assume that the rest of the charge was also consumed by liquid product formation, which, at least in part, was trapped in the GDE. Additionally, the gas outlet of the microfluidic flow cell was coupled to a liquid/gas separation unit (to protect the residual gas analyzer and the GC), adding a buffer to the system. These two factors together lead to a slight underestimation of the amount of the formed products. We also mention that – even though we could not detect – other products might also form during CORR.[58]

The total FE remained well below 100% when the CST content was increased to values over 15%. It is visible that in some cases, we were only able to account for approximately 25–50% of the passed charge (Fig. S10, ESI†). This phenomenon was accompanied by a notably more vigorous bubble formation in the outlet liquid electrolyte stream as compared to measurements with lower CST content GDEs at identical current densities. Based on this, we assumed that cathodic gas phase products transport to the liquid stream, in this case, instead of exiting the electrolyzer cell with the remnant CO. To determine the composition and the quantity of the gas in the outlet liquid stream, the gas and liquid outlet of the electrolyzer cell was connected downstream of the electrolyzer cell to a liquid/gas separator (for the schematic representation, see Fig. S11, ESI†). This setup allowed us to quantify the formed gas-phase products in the gas and liquid phases together. Almost no additional gas phase products were detected when the CST content remained below 20 wt% (Fig. 2D). On the other hand, if the CST content was higher than that, almost all missing FE was consumed by H_2 formation (and this H_2 left the cell with the liquid stream). Interestingly, similar results were found for the CLs comprised of the pristine Cu NPs without any additive. While the observed trends for the samples containing a high amount of CST coincide with the one measured for the pristine Cu, we speculate that two separate mechanisms are responsible (Scheme 1). As it was presented in Fig. 2A, Cu NPs (without the addition of any binder) are more hydrophilic in nature when they get in contact with 1 M KOH electrolyte. As a result of this, the GDL gradually gets flooded (even at the lowest applied current density) under electrolysis conditions, resulting in the predominant formation of H_2. To gain further insights, dynamic contact angle measurements were performed (Fig. 3A–C). On top of static contact angle values, these measurements provide merit on the infiltration of the electrolyte solution in the GDE over time. This causes hysteresis in the measured contact angles when increasing and subsequently decreasing the volume of the liquid droplet (advancing and receding contact angles, accordingly).

A large hysteresis was seen with the carbon GDL. Such dynamic contact angle measurements were not even possible for the binder-free catalyst layer because the KOH solution

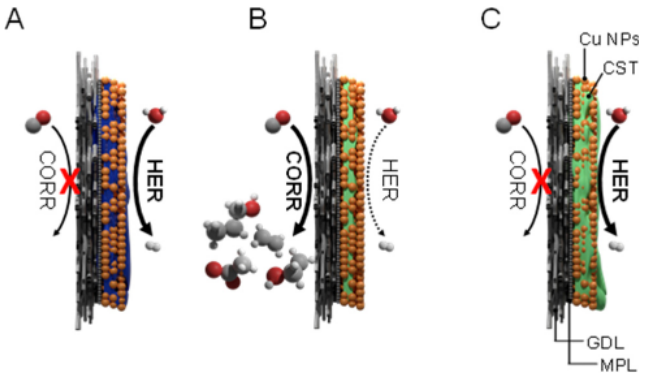

Scheme 1 Schematic structure of the GDE at different binder contents. Without binder, the catalyst layer is flooded (A), as it is also indicated by the contact angle measurements, shown in Fig. 2A. At optimal binder content, the reactant CO reaches the catalyst surface, and the formed products leave the cell with the remnant CO gas (B). At too high binder content, the CO reactant cannot reach the catalyst surface, therefore, H_2 evolves at the catalyst/liquid electrolyte interface (C).

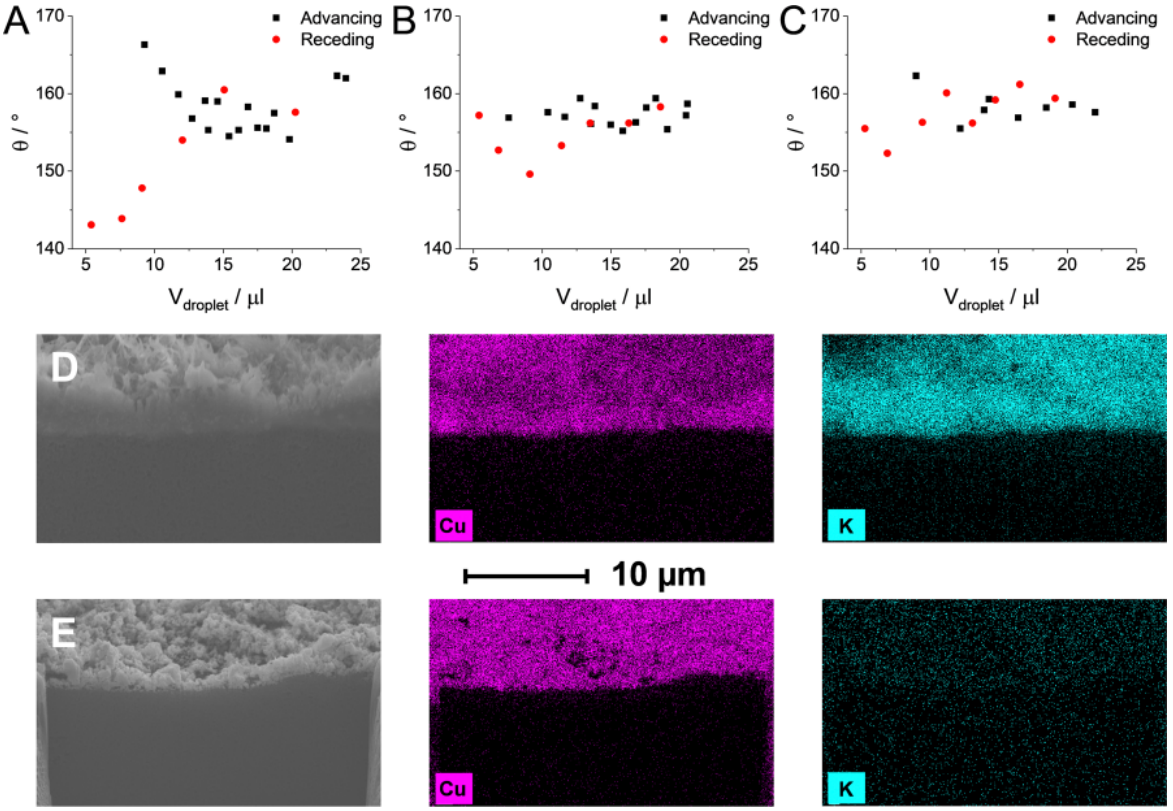

Fig. 3 Dynamic contact angle measurements with a 1 M KOH solution on a (A) pure H23C6 GDL, (B) 5 wt% CST containing Cu based GDE and a (C) 30 wt% CST containing Cu based GDE. Cross-sectional SEM EDX images of the catalyst layer and the microporous layer of the GDL, showing the structure, the copper and potassium content of a (D) CST-free Cu GDE and a (E) 5 wt% CST containing Cu GDE.

almost immediately fully penetrated it. In contrast, almost no hysteresis, hence no notable electrolyte solution penetration was experienced with the CST containing GDEs. To better visualize the electrolyte solution penetration, we formed a V = 500 µl 1 M KOH droplet on a CST-free Cu GDE and a 5% CST-containing Cu GDE and let it penetrate for 10 minutes. Subsequently, the excess liquid was wiped gently, the sample was dried, and FIB-SEM-EDX experiments were performed on the different samples (Fig. 3D and E). These revealed that the CST-free Cu layer was fully impregnated by the electrolyte solution after the 10 minute contact time, while a negligible amount of potassium ions was seen in the 5% CST-containing sample. Note that this measurement directly samples the whole catalyst layer and not only the topmost layer(s).

Therefore, the case of CST-containing GDEs is more complicated. The microenvironment (*i.e.*, hydrophobicity) around the Cu NPs can be effectively tailored by the introduction of CST in the CL. If the CST loading is in the proper range (5–15 wt%), optimal conditions are created, allowing the selective reduction of CO in parallel with suppressed HER. Importantly, CST does not fully cover the surface of the CL, and no coherent layer formation was observed on the SEM images (see Fig. S1, ESI†). Furthermore, contact angles measured for the samples containing CST in 5–15 wt% decreased to the range of what was measured for the Cu NPs without CST after constant current electrolysis performed at j = 300 mA cm^{-2} (Fig. 2A). This also excludes a coherent film formation on the surface of the CL and suggests that the Cu NPs in the topmost part of the CL are not fully wrapped by the polymer and are accessible for the electrolyte solution. In contrast, a high contact angle and a superhydrophobic character were measured for the electrodes containing at least 20 wt% CST, even after using these in CORR. This is reasoned by the coherent polymer film formation (Fig. S1, ESI†) on the top of the CL, dictating the surface wetting properties. As concluded from the QCM data (Fig. S4, ESI†), the introduction of CST in the CL had no effect on the reactant adsorption. Hence, we attribute only a physical effect to its presence, namely, altering the hydrophobicity at the catalyst/electrolyte interface. Furthermore, the addition of even the smallest amount of CST highly stabilized the CL mechanically, preventing catalyst detachment during electrolysis. The coordination of CST to the Cu catalyst is driven by both a charge compensation and a physical interaction – based on our measurements, a negative ζ-potential was recorded for the dispersed Cu nanoparticles. This is compensated by the CST polymer at *ca.* 0.15 w% CST content (Fig. S12, ESI†). Above this amount, the CST might adsorb on the catalyst surface by means of physical interaction, and this excess polymer aids the mechanical stability of the formed CL. When a large amount of CST was added, part of the polymer is bound to the surface of the catalyst particles, but some portion was not, the polymer was in excess. According to top-down SEM

images, at high CST content, the polymer is present at the surface of the CL, too, forming a coherent layer (Fig. S1, ESI†).

The compact layer formation is in line with the contact angles measured for the 20–30 wt% CST-containing samples after electrolysis (Fig. 2A), showing an unaltered value as compared with the fresh samples. The coherent polymer film formation also explains the larger cell voltages at high CST contents as the electrical resistance of the GDE increases (Fig. S7, ESI†). Similarly, at high polymer content CST might also accumulate at the interface between the GDL and the CL, hindering the gas transport to the CL. The charge still passes, but HER prevails instead of CORR because of the absence of CO in the close vicinity of the catalyst. Based on our detailed FIB SEM studies (Fig. 3D and E) and N_2 gas adsorption experiments (not shown here), we could not observe any polymer infiltration in the GDL. Hence the low CORR selectivity at high polymer contents is related to the interfaces between the CL and the solution/GDL, as well as to the structure of the CL. The presence of the polymer binder at the surface of the Cu nanoparticles might also affect the overall pore structure of the catalyst layer. Porosity was shown to influence the CO_2RR selectivity of, for example, N-doped nanocarbon electrodes.[59] We think that hydrophobicity and pore structure can both have an influence on catalysts selectivity in CORR too.

The performance of the CST-modified samples was compared with binders, widely applied in the literature to tailor the hydrophobicity of the CL.[44] We have performed experiments with frequently applied anion exchange ionomers, that ensured high performance in our earlier experiments in zero-gap electrolyzer cells,[6,27] but we always experienced the rapid flooding of the cathode GDE. In other experiments, CST was replaced with Nafion, and samples with varying Nafion content (between 5–30 wt%, the same range as in the case of CST) were prepared. A set of chronovoltammetry curves (recorded for the sample containing 5 wt% Nafion) along with the product distribution is presented in Fig. S13 (ESI†). The measured cell voltages are similar to the ones measured for the Cu NPs/CST system, along with the set of the formed products. Importantly, H_2 formation was only slightly suppressed in the presence of Nafion compared to the binder-free Cu nanoparticles. Samples prepared with a Nafion content between 5–15 wt% showed the highest selectivity toward CORR. Interestingly, when the Nafion content was above 5 wt%, the C_{2+} formation rate gradually increased until 4–500 mA cm^{-2} total current density, where partial current densities suddenly dropped, probably due to the flooding of the GDE (see examples where flooding occurred in Fig. S14, ESI†). Flooding was also confirmed by analyzing the gas products present in the gas and liquid outlet streams of the electrolyzer cell (Fig. S15, ESI,† similar to Fig. 2D), where hydrogen evolution was witnessed almost exclusively at higher current densities. Flooding of the cathode GDE not only manifested in the drop of the cell voltage but it was accompanied by the decrease of the total detected FE values when either Nafion or PTFE or a high amount (above 20 wt%) CST were applied as binders (see the exact values in Table S2, ESI†). As discussed earlier in the manuscript, most of the formed hydrogen in these cases exited the cell with the liquid stream instead of the gas outlet of the cell, hence the observed low total FEs in Fig. 3 and Fig. S15 (ESI†).

A further strategy to increase the hydrophobicity of the CL is the addition of PTFE nanoparticles to the Cu NPs dispersion prior to spray-coating[27] or to pre-treat the GDL prior to the immobilization of the CL with a PTFE dispersion.[44] In our study, the first approach was used, and no additional binder was applied besides the PTFE NPs (Fig. S16, ESI†). The trends in terms of cell voltages differ from the ones observed in the Nafion- and CST-containing CL cases. While the first experiment at the lowest current density is similar to the other cases, the cell voltage rapidly increases during the second measurement. This is accompanied by the appearance of small dark brown particles in the electrolyte outlet stream, suggesting the mechanical decomposition of the CL during electrolysis. Such degradation was observed for all samples, independent from the PTFE loading. The cell voltage did not change significantly at higher current densities suggesting the excessive formation of H_2, while almost no CORR products were detected.

Fig. 4 compares the formation rates of both H_2 and all CORR products with and without the different additives at 500 mA cm^{-2}

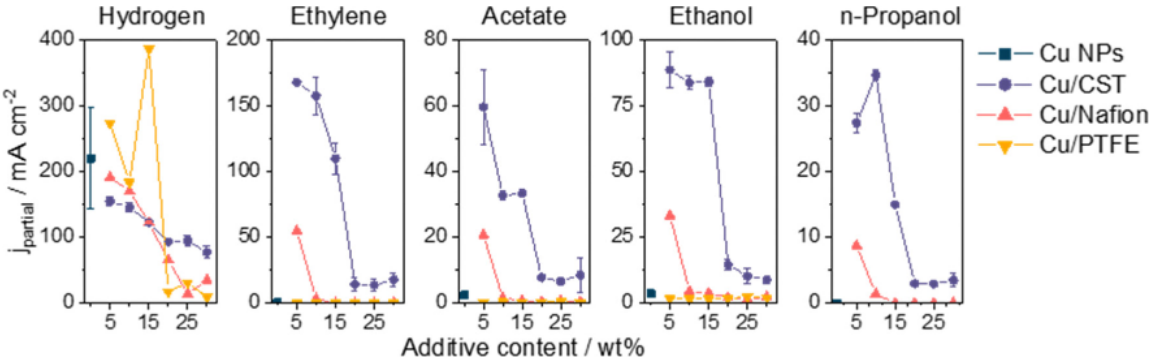

Fig. 4 Product distribution measured with Cu NP GDEs containing different additives: no additive, CST, Nafion, and PTFE. Data were recorded by applying 500 mA cm^{-2} current density in 1 M KOH electrolyte solution. The electrolyte flow rate was set to 0.5 cm^3 min^{-1} while the CO flow rate was 26.5 sccm. The amount of the given additive was always between 5–30 wt%. Error bars for the Cu NPs and Cu/CST samples were calculated from at least two individual measurements, each performed on a fresh cathode GDE. The lines among the data points serve only as a guide to the eyes.

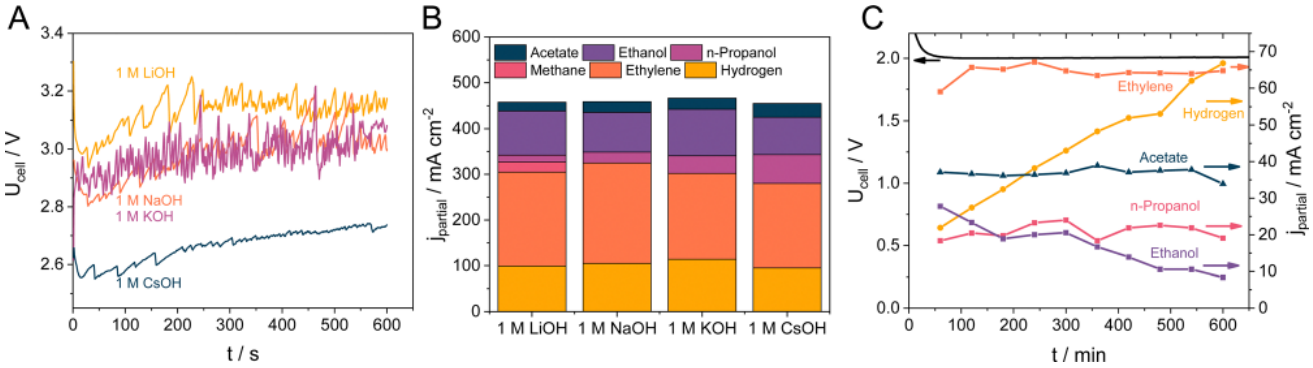

Fig. 5 (A) Chronovoltammetric curves and (B) product formation rates during CO electrolysis using a Cu NPs + 5 wt% CST sample, at j = 500 mA cm^{-2} current density, applying different electrolyte solutions. (C) Product distribution during a long-term CO electrolysis at j = 200 mA cm^{-2}, using a Cu NPs + 5 wt% CST sample and a 5 M KOH electrolyte solution. The electrolyte flow rate was 1 cm^3 min^{-1} while the CO feed rate was maintained at 26.5 sccm in all experiments.

current density. The amount of formed H_2 is similar in the case of the Nafion-, and CST-containing samples, while it is notably higher in the presence of PTFE in the CL. In terms of the CORR products, ethylene was only detected when the CL contained 5 wt% Nafion in the case of the Cu/Nafion system, while more than three times higher partial current densities were obtained with the Cu/CST samples with the optimal CST content (5–10 wt%). This observation underlines that while the addition of Nafion was clearly beneficial to the CORR activity, the GDEs gradually got flooded over the course of the electrolysis (Fig. S14 and S15, ESI†). Similar conclusions can be made regarding the liquid CORR products; the Cu/CST system outperformed its pristine, Cu/Nafion, and Cu/PTFE counterparts.

Effect of the electrolyte on the activity and selectivity, long-term operation

Further experiments were performed with the 5 wt% CST containing GDEs, as these showed the most promising results during the initial screening. As for the electrolyte concentration and pH, the nature of the alkali cation is often claimed to affect the reaction rate and selectivity. Hence, we performed CORR experiments using different electrolyte solutions at j = 500 mA cm^{-2} current density. Fig. 5A shows that the nature of the electrolyte has a notable influence on the cell voltage. While the cell voltage is around 3.0 V for the measurements performed in 1 M NaOH and KOH, it is approximately 100 mV higher when LiOH was used as an electrolyte. In contrast, when the electrolyte was changed to 1 M CsOH the cell voltage dropped by 300 mV to around 2.7 V. These differences are also reflected in the product distribution: the amount of H_2 is the highest for the measurements in 1 M LiOH, while the amount of hydrogen is similar in the case of 1 M KOH, NaOH and CsOH (Fig. 5B). This similarity does not stand for the formation rate of C_2H_4 as that followed the NaOH > LiOH > KOH > CsOH order. Besides H_2 and C_2H_4, CH_4 was also detected as a gas phase product when LiOH was applied as the electrolyte. As for the liquid products, the formation rate of ethanol is the highest for KOH and NaOH, while the amount of formed *n*-propanol and acetate monotonously increases in the order of LiOH < NaOH < KOH < CsOH, reaching a maximum of 63 and 30 mA cm^{-2} partial current density, respectively.

The stability of the CORR process was monitored for 10 hours at j = 200 mA cm^{-2} in a 5 M KOH electrolyte solution. As shown in Fig. 5C, the ethylene formation rate (along with the partial current densities for *n*-propanol and acetate) remained relatively stable within the timeframe of the measurement, with FEs of 32 ± 1%, 10.5 ± 1% and 18.4 ± 0.6% for ethylene, *n*-propanol, and acetate, respectively. In contrast, partial current densities for ethanol formation decreased from 28 to around 8.3 mA cm^{-2}, while the hydrogen production rate increased from 22 to 66 mA cm^{-2}. We relate this latter effect to the morphological changes of the catalyst particles, distorting the structure of the CL (note the changes in the catalyst morphology on the SEM images in Fig. S17, ESI†), allowing more water to enter the GDE. Such morphological change in copper catalysts is well-known from CO_2RR and CORR studies, and therefore it points beyond the scope of our current study. Most importantly, however, no flooding was observed during the measurements, proving the applicability of the Capstone ST-110 as a cathodic catalyst binder for CORR. We note here that the stability depends on a wealth of different parameters (physical degradation of the CL/GDE due to the leaching, restructuring of the catalyst, change of hydrophobicity, precipitation of salts, durability of cell components from the membrane to the current collectors, *etc.*),[60] which must be concurrently optimized to ensure stable long-term operation. In this contribution, the prime focus was on tailoring the wetting properties (*i.e.*, hydrophobic character) of the GDE; the lifetime of the CORR cell could be substantially improved by optimizing these parameters. This is expected to be greatly aided by using sophistically designed catalysts, such as atomically dispersed copper or specifically engineered copper surfaces,[61,62] in combination with the presented CST binder.

Conclusions

A new polymer binder (Capstone ST-110) was presented for controlling the microenvironment of Cu nanoparticle catalysts

in gas diffusion electrodes for electrochemical CO reduction. Using this low-cost, commercially available pore sealer, we could achieve above 70% C_{2+} selectivity even at high current densities. Importantly, no specific interaction between the polymer and the CO reactant gas was detected. This suggests that the observed beneficial effect is related to the microscopic hydrophobicity of the catalyst particles due to the fluoropolymer coating on their surface. These findings point out that polymers that form thin films on the catalyst surface (instead of forming nanoparticles that are incorporated among the catalyst particles, *e.g.*, PTFE) might be suitable binders for CORR. Exploring such cost-efficient, chemically stable polymers might be a promising avenue for future studies on electrochemical CO reduction.

Author contributions

Attila Kormányos: methodology, validation, investigation, data curation, writing – original draft, visualization. Balázs Endrődi: conceptualization, data curation, writing – original draft, supervision. Zheng Zhang: methodology, validation, investigation. Angelika Samu: methodology, validation, investigation. László Mérai: investigation. Gergely F. Samu: investigation. László Janovák: investigation, resources, data curation. Csaba Janáky: conceptualization, resources, writing – review & editing, supervision, funding acquisition.

Conflicts of interest

There are no conflicts to declare.

Acknowledgements

This project has received funding under the European Union's Horizon Europe research and innovation program from the European Research Council (ERC, Grant Agreement No. 101043617) and the FlowPhotoChem project (Grant Agreement No. 862453). We also thank the Hungarian Renewable Energy National Laboratory for support, financed by the RRF-2.3.1-21- 2022-00009 project. B. E., L. J., G. F. S., and A. K. also acknowledge financial support from the János Bolyai Research Scholarship of the Hungarian Academy of Sciences. This work was further supported by the National Research, Development, and Innovation Office (NKFIH) through the FK-132564 project. The ELI ALPS project (GINOP-2.3.6-15-2015-00001) is supported by the European Union and co-financed by the European Regional Development Fund. Egon Kecsenovity is acknowledged for his contribution to designing the electrolyzer cell and for taking the TEM images.

Notes and references

1 M. Jouny, G. S. Hutchings and F. Jiao, *Nat. Catal.*, 2019, **2**, 1062–1070.
2 H. Zhang, J. Li, M. J. Cheng and Q. Lu, *ACS Catal.*, 2019, **9**, 49–65.
3 A. A. Samu, A. Kormányos, E. Kecsenovity, N. Szilágyi, B. Endrődi and C. Janáky, *ACS Energy Lett.*, 2022, **7**, 1859–1861.
4 R. E. Clarke, S. Giddey, F. T. Ciacchi, S. P. S. Badwal, B. Paul and J. Andrews, *Int. J. Hydrogen Energy*, 2009, **34**, 2531–2542.
5 I. E. L. Stephens, K. Chan, A. Bagger, S. W. Boettcher, J. Bonin, E. Boutin, A. K. Buckley, R. Buonsanti, E. R. Cave, X. Chang, S. W. Chee, A. H. M. da Silva, P. de Luna, O. Einsle, B. Endrődi, M. Escudero-Escribano, J. V. Ferreira de Araujo, M. C. Figueiredo, C. Hahn, K. U. Hansen, S. Haussener, S. Hunegnaw, Z. Huo, Y. J. Hwang, C. Janáky, B. S. Jayathilake, F. Jiao, Z. P. Jovanov, P. Karimi, M. T. M. Koper, K. P. Kuhl, W. H. Lee, Z. Liang, X. Liu, S. Ma, M. Ma, H.-S. Oh, M. Robert, B. R. Cuenya, J. Rossmeisl, C. Roy, M. P. Ryan, E. H. Sargent, P. Sebastián-Pascual, B. Seger, L. Steier, P. Strasser, A. S. Varela, R. E. Vos, X. Wang, B. Xu, H. Yadegari and Y. Zhou, *J. Phys.: Energy*, 2022, **4**, 042003.
6 B. Endrődi, E. Kecsenovity, A. Samu, T. Halmágyi, S. Rojas-Carbonell, L. Wang, Y. Yan and C. Janáky, *Energy Environ. Sci.*, 2020, **13**, 4098–4105.
7 S. S. Bhargava, F. Proietto, D. Azmoodeh, E. R. Cofell, D. A. Henckel, S. Verma, C. J. Brooks, A. A. Gewirth and P. J. A. Kenis, *ChemElectroChem*, 2020, **7**, 2001–2011.
8 Z. Xing, X. Hu and X. Feng, *ACS Energy Lett.*, 2021, **6**, 1694–1702.
9 M. G. Kibria, J. P. Edwards, C. M. Gabardo, C. Dinh, A. Seifitokaldani, D. Sinton and E. H. Sargent, *Adv. Mater.*, 2019, **31**, 1807166.
10 G. O. Larrazábal, P. Strøm-Hansen, J. P. Heli, K. Zeiter, K. T. Therkildsen, I. Chorkendorff and B. Seger, *ACS Appl. Mater. Interfaces*, 2019, **11**, 41281–41288.
11 H. Yang, J. J. Kaczur, S. D. Sajjad and R. I. Masel, *J. CO2 Util.*, 2020, **42**, 101349.
12 J. A. Rabinowitz and M. W. Kanan, *Nat. Commun.*, 2020, **11**, 5231.
13 Y. Hori, A. Murata, R. Takahashi and S. Suzuki, *Chem. Lett.*, 1987, 1665–1668.
14 Y. Hori, R. Takahashi, Y. Yoshinami and A. Murata, *J. Phys. Chem. B*, 1997, **101**, 7075–7081.
15 J. Li, Z. Wang, C. McCallum, Y. Xu, F. Li, Y. Wang, C. M. Gabardo, C.-T. Dinh, T.-T. Zhuang, L. Wang, J. Y. Howe, Y. Ren, E. H. Sargent and D. Sinton, *Nat. Catal.*, 2019, **2**, 1124–1131.
16 R. Xia, J. J. Lv, X. Ma and F. Jiao, *J. Catal.*, 2021, **398**, 185–191.
17 M. Jouny, W. Luc and F. Jiao, *Nat. Catal.*, 2018, **1**, 748–755.
18 G. L. De Gregorio, T. Burdyny, A. Loiudice, P. Iyengar, W. A. Smith and R. Buonsanti, *ACS Catal.*, 2020, **10**, 4854–4862.
19 T. Liu, J. Sang, H. Li, P. Wei, Y. Zang and G. Wang, *Battery Energy*, 2022, **1**, 20220012.
20 L. Zaza, K. Rossi and R. Buonsanti, *ACS Energy Lett.*, 2022, **7**, 1284–1291.
21 Y. Li, Y. Qian, Y. Ji, H. Li and Y. Liu, *J. Mater. Chem. A*, 2019, **7**, 24000–24004.

22 Y. Liu, H. Jiang and Z. Hou, *Angew. Chem., Int. Ed.*, 2021, **60**, 11133–11137.
23 A. O. Elnabawy, J. Schumann, P. Bothra, A. Cao and J. K. Nørskov, *Top. Catal.*, 2020, **63**, 635–648.
24 S.-F. Zhao, M. Horne, A. M. Bond and J. Zhang, *J. Phys. Chem. C*, 2016, **120**, 23989–24001.
25 D. V. Vasilyev and P. J. Dyson, *ACS Catal.*, 2021, **11**, 1392–1405.
26 J. Li, X. Li, C. M. Gunathunge and M. M. Waegele, *Proc. Natl. Acad. Sci. U. S. A.*, 2019, **116**, 9220–9229.
27 B. Endrődi, A. Samu, E. Kecsenovity, T. Halmágyi, D. Sebők and C. Janáky, *Nat. Energy*, 2021, **6**, 439–448.
28 J. Resasco, L. D. Chen, E. Clark, C. Tsai, C. Hahn, T. F. Jaramillo, K. Chan and A. T. Bell, *J. Am. Chem. Soc.*, 2017, **139**, 11277–11287.
29 S. Ringe, E. L. Clark, J. Resasco, A. Walton, B. Seger, A. T. Bell and K. Chan, *Energy Environ. Sci.*, 2019, **12**, 3001–3014.
30 J. Li, D. Wu, A. S. Malkani, X. Chang, M. Cheng, B. Xu and Q. Lu, *Angew. Chem.*, 2020, **132**, 4494–4499.
31 A. Guan, Q. Wang, Y. Ji, S. Li, C. Yang, L. Qian, L. Zhang, L. Wu and G. Zheng, *J. Mater. Chem. A*, 2021, **9**, 21779–21784.
32 T. Burdyny and W. A. Smith, *Energy Environ. Sci.*, 2019, **12**, 1442–1453.
33 H. Rabiee, L. Ge, X. Zhang, S. Hu, M. Li and Z. Yuan, *Energy Environ. Sci.*, 2021, **14**, 1959–2008.
34 M. Li, M. N. Idros, Y. Wu, T. Burdyny, S. Garg, X. S. Zhao, G. Wang and T. E. Rufford, *J. Mater. Chem. A*, 2021, **9**, 19369–19409.
35 N. J. Shirtcliffe, G. McHale, M. I. Newton and C. C. Perry, *Langmuir*, 2005, **21**, 937–943.
36 M. E. Leonard, M. J. Orella, N. Aiello, Y. Román-Leshkov, A. Forner-Cuenca and F. R. Brushett, *J. Electrochem. Soc.*, 2020, **167**, 124521.
37 M. E. Leonard, L. E. Clarke, A. Forner-Cuenca, S. M. Brown and F. R. Brushett, *ChemSusChem*, 2020, **13**, 400–411.
38 Y. Jännsch, M. Hämmerle, E. Simon, M. Fleischer and R. Moos, *Energy Technol.*, 2022, 2200046.
39 Y. Ma, J. Wang, J. Yu, J. Zhou, X. Zhou, H. Li, Z. He, H. Long, Y. Wang, P. Lu, J. Yin, H. Sun, Z. Zhang and Z. Fan, *Matter*, 2021, **4**, 888–926.
40 C. Kim, J. C. Bui, X. Luo, J. K. Cooper, A. Kusoglu, A. Z. Weber and A. T. Bell, *Nat. Energy*, 2021, **6**, 1026–1034.
41 X. Zhou, H. Liu, B. Y. Xia, K. (Ken) Ostrikov, Y. Zheng and S. Qiao, *SmartMat*, 2022, **3**, 111–129.
42 J. C. Bui, C. Kim, A. J. King, O. Romiluyi, A. Kusoglu, A. Z. Weber and A. T. Bell, *Acc. Chem. Res.*, 2022, **55**, 484–494.
43 A. Venugopal, L. H. T. Egberts, J. Meeprasert, E. A. Pidko, B. Dam, T. Burdyny, V. Sinha and W. A. Smith, *ACS Energy Lett.*, 2022, **7**, 1586–1593.
44 R. Chen, H. Su, D. Liu, R. Huang, X. Meng, X. Cui, Z. Tian, D. H. Zhang and D. Deng, *Angew. Chem.*, 2020, **132**, 160–166.
45 C. W. Li, J. Ciston and M. W. Kanan, *Nature*, 2014, **508**, 504–507.
46 Y. Ji, C. Yang, L. Qian, L. Zhang and G. Zheng, *J. Colloid Interface Sci.*, 2021, **600**, 847–853.
47 D. Wakerley, S. Lamaison, F. Ozanam, N. Menguy, D. Mercier, P. Marcus, M. Fontecave and V. Mougel, *Nat. Mater.*, 2019, **18**, 1222–1227.
48 X. Chen, J. Chen, N. M. Alghoraibi, D. A. Henckel, R. Zhang, U. O. Nwabara, K. E. Madsen, P. J. A. Kenis, S. C. Zimmerman and A. A. Gewirth, *Nat. Catal.*, 2021, **4**, 20–27.
49 Y. Cheng, J. Hou and P. Kang, *ACS Energy Lett.*, 2021, **6**, 3352–3358.
50 D. T. Whipple, E. C. Finke and P. J. A. Kenis, *Electrochem. Solid-State Lett.*, 2010, **13**, B109.
51 B. Kim, S. Ma, H.-R. Molly Jhong and P. J. A. Kenis, *Electrochim. Acta*, 2015, **166**, 271–276.
52 K. P. Kuhl, E. R. Cave, D. N. Abram and T. F. Jaramillo, *Energy Environ. Sci.*, 2012, **5**, 7050–7059.
53 R. B. Kutz, Q. Chen, H. Yang, S. D. Sajjad, Z. Liu and I. R. Masel, *Energy Technol.*, 2017, **5**, 929–936.
54 J. Wang, Y. Zhao, B. P. Setzler, S. Rojas-Carbonell, C. Ben Yehuda, A. Amel, M. Page, L. Wang, K. Hu, L. Shi, S. Gottesfeld, B. Xu and Y. Yan, *Nat. Energy*, 2019, **4**, 392–398.
55 D. Hursán, A. Kormányos, K. Rajeshwar and C. Janáky, *Chem. Commun.*, 2016, **52**, 8858–8861.
56 P. Grosse, D. Gao, F. Scholten, I. Sinev, H. Mistry and B. Roldan Cuenya, *Angew. Chem., Int. Ed.*, 2018, **57**, 6192–6197.
57 N. S. Romero Cuellar, K. Wiesner-Fleischer, M. Fleischer, A. Rucki and O. Hinrichsen, *Electrochim. Acta*, 2019, **307**, 164–175.
58 Y. Zhou, R. Ganganahalli, S. Verma, H. R. Tan and B. S. Yeo, *Angew. Chem., Int. Ed.*, 2022, 1–8.
59 D. Hursán, A. A. Samu, L. Janovák, K. Artyushkova, T. Asset, P. Atanassov and C. Janáky, *Joule*, 2019, **3**, 1719–1733.
60 U. O. Nwabara, E. R. Cofell, S. Verma, E. Negro and P. J. A. Kenis, *ChemSusChem*, 2020, **13**, 855–875.
61 Y. Zhao, X. Chang, A. S. Malkani, X. Yang, L. Thompson, F. Jiao and B. Xu, *J. Am. Chem. Soc.*, 2020, **142**, 9735–9743.
62 X. Fu, Y. Wang, H. Shen, Y. Yu, F. Xu, G. Zhou, W. Xie, R. Qin, C. Dun, C.-W. Pao, J.-L. Chen, Y. Liu, J. Guo, Q. Yue, J. J. Urban, C. Wang and Y. Kang, *Mater. Today Phys.*, 2021, **19**, 100418.